Biochemistry and Biophysics Reports 46 (2026) 102614

Contents lists available at ScienceDirect

Biochemistry and Biophysics Reports

journal homepage: www.elsevier.com/locate/bbrep

Long-read transcriptomic profiling of a glioma cell line following m6A regulator perturbations

Hanna Lee [1], Syeda Maheen Batool [1,2], Ana K. Escobedo [1], Denalda Gashi, Kesli Faber, Pavithra Ponnolu, Nina R. Barretts, Prerna Khanna [3], Kase D. Haas, Tiffaney Hsia [4], Bob S. Carter [5], Leonora Balaj [*]

Department of Neurosurgery, Massachusetts General Hospital, Harvard Medical School, Boston, MA, USA

ARTICLE INFO

Keywords:
N6-methyladenosine (m6A)
RNA
Epitranscriptomics
Isoform
Alternative splicing
Signaling
Glioma

ABSTRACT

N6-methyladenosine (m6A) is the most prevalent internal mRNA modification and is enriched in the central nervous system (CNS), yet its role in glioma remains incompletely defined. Using long-read direct RNA sequencing, we mapped transcriptome-wide m6A modifications in a single glioma cell line following targeted knockdown of the m6A reader IGF2BP2, writer METTL3, and eraser ALKBH5. Across perturbations, the global architecture of m6A, including transcript class, positional enrichment, and site multiplicity, was largely preserved, while differential methylation was weakly coupled to gene expression. In contrast, m6A regulator perturbation coincided with widespread isoform switching and with changes in untranslated regions, coding potential, and predicted transcript fate, largely independent of bulk gene expression changes. Public glioma datasets further supported the relevance of isoform-specific changes in glioma. Together, these findings highlight isoform-level transcript variation associated with m6A regulator perturbation and support the use of long-read, isoform-resolved approaches to study RNA regulatory states in glioma.

1. Introduction

Over 163 RNA modifications have been identified, with N6-methyladenosine (m6A) the most prevalent modification detected in diverse RNA types (mRNA, tRNA, rRNA, circRNA, miRNA, lncRNA) [1]. m6A modification is dynamically regulated by three distinct groups of binding proteins, collectively termed m6A regulators: writers (methyltransferases), readers (m6A-binding proteins), and erasers (demethylases) which work together to maintain a dynamic balance in RNA modification [1]. Of all these regulators, m6A has been implicated in multiple aspects of RNA metabolism including alternative splicing, transcript stability, localization and translation [2,3].

m6A regulation has been extensively studied in both physiological and pathological contexts, including malignancies of hematopoietic, reproductive systems and central nervous system [4]. Notably m6A has been reported to be more abundant in the CNS relative to other organs [4] and plays a central role in development [5,6] and dysfunction [7,8]. Glioma is the most common primary CNS tumor, with glioblastoma being the most aggressive subtype [9]. Tumor recurrence and treatment resistance contribute to the poor prognosis of these heterogeneous lesions, with a median survival of approximately 15 months [9–11]. Emerging evidence links m6A to glioma biology through effects on tumor progression [12], stemness [13–15], tumor cell proliferation [16] and modulation of the tumor microenvironment [17,18]. Conversely, other studies have demonstrated anticancer effects of m6A regulators, with lower m6A levels promoting tumorigenesis of glioma stem cells (GSCs) [19]. Together, these findings are suggestive of a potential dual, context-dependent role of m6A in glioma, underscoring the need for a more detailed exploration of its molecular mechanisms. A major limitation of prior studies is the reliance on short-read sequencing

* Corresponding author. 185 Cambridge St., Boston, MA, USA.
E-mail address: Balaj.Leonora@mgh.harvard.edu (L. Balaj).
[1] co-first authors.
[2] Current address: University of Oklahoma, College of Medicine, Oklahoma City, OK, USA.
[3] Current address: University of Edinburgh, Medical School, Edinburgh, UK.
[4] Current address: University of Massachusetts, Chan Medical School, Worcester, MA, USA.
[5] University of Utah Health, Salt Lake City, UT, USA.

https://doi.org/10.1016/j.bbrep.2026.102614
Received 6 April 2026; Received in revised form 28 April 2026; Accepted 30 April 2026

approaches, which obscure transcript isoform structure [5,20] and limit resolution of how m6A influences RNA regulatory states beyond bulk gene expression. Whether m6A primarily exerts its effects through global transcriptional control or through selective, isoform-specific modulation of RNA fate remains unclear [5,21].

Here, we investigated the molecular consequences of perturbing m6A regulatory machinery in a glioma cell model using long-read direct RNA sequencing. We generated knockdown models targeting the m6A reader IGF2BP2, the writer METTL3, and the eraser ALKBH5, alongside a scrambled siRNA control. Using Oxford Nanopore–based direct RNA sequencing with replicate profiling, we mapped m6A modifications at single-nucleotide resolution while preserving full-length transcript information. This approach enabled an integrated analysis of m6A distribution, gene expression, and isoform usage, providing insight into how m6A regulation manifests at the transcriptome level in glioma.

2. Methods

2.1. Cell line experimental procedures

2.1.1. Nanopore sequencing experiments

The human glioma cell line Gli36 (generated at Massachusetts General Hospital under approved IRB procedures) was used for transcriptome-wide m6A profiling by nanopore sequencing. Knockdown (KD) of m6A regulators was performed using siRNA-mediated transfection. The following experimental conditions were included: (i) naïve (no treatment), (ii) ALKBH5 (eraser) KD, (iii) IGF2BP2 (reader) KD, (iv) METTL3 (writer) KD, and (v) scrambled siRNA control. Three technical replicates were generated per condition, resulting in a total of N = 15 nanopore sequencing runs, which constituted the primary dataset for downstream analyses.

2.1.2. qPCR validation experiments

For independent validation of differential isoform usage identified from the nanopore sequencing analysis, the Gli36 cell line was again used, and knockdown of additional m6A regulators was performed via siRNA transfection. Experimental conditions included: (i) naïve (no treatment), (ii) ALKBH5 (eraser) KD, (iii) IGF2BP2 (reader) KD, (iv) METTL3 (writer) KD, (v) FTO (eraser) KD, (vi) YTHDF2 (reader) KD, (vii) METTL14 (writer) KD, and (viii) scrambled siRNA control. Two technical replicates were performed per condition, yielding a total of N = 16 qPCR runs.

2.2. Selected silencer RNA (siRNA) for m6A regulator knockdown

Select Pre-designed siRNAs (Catalog Number: 4427037) were purchased from ThermoFisher Scientific for knockdown of known m6A regulators: ALKBH5 (siRNA ID: s29688), IGF2BP2 (siRNA ID: s20924), METTL3 (siRNA ID: s32142), FTO (siRNA ID: s35511), YTHDF2 (siRNA ID: s28147) and METTL14 (siRNA ID: s33681).

2.3. Cell line transfection and collection

On Day 0 (one day before transfection), 2 x 105 Gli36EGFRvIII cells were plated in a 6-well plate using Opti-MEMTM reduced serum medium (ThermoFisher Scientific, Waltham, MA, USA). The following day, cells were checked to ensure 60-80% confluency prior to transfection. Transfection on Day 1 was performed using Lipofectamine RNAiMAX Reagent (ThermoFisher Scientific, Waltham, MA, USA) according to manufacturer's instructions. Briefly, both lipofectamine RNAiMAX reagent and silencer RNA (siRNA) concentrates were diluted in Opti-MEM medium. A volume of 3 μl of 10 μM siRNA was combined with 150 μl of Opti-MEM medium to achieve a final concentration of 30 pmol. RNA-lipid complexes were then prepared by combining diluted siRNA and diluted lipofectamine RNAiMAX reagent in a 1:1 ratio followed by 5 min incubation at room temperature. The siRNA-lipid complex was then added to the individual wells of the 6 well plate, and gently rocked back and forth to mix. Cells were transfected for 48h at 37 °C in a CO2 incubator to achieve optimal m6A regulator knockdown. On Day 3, the Opti-MEM medium was carefully aspirated and replaced with Dulbecco's Modified Eagle Medium (DMEM, Invitrogen, Waltham, MA) with high glucose containing 10% fetal bovine serum (FBS; Life Technologies Corporation, Carlsbad, CA, USA) and 1% Penicillin/Streptomycin solution (Pen/Strep; Life Technologies Corporation, Carlsbad, CA, USA). Transfected cells were cultured in DMEM for 24h and transferred to T-75 flask on Day 4. On Day 7, cells were transferred to Nunc™ TripleFlask™ Treated Cell Culture Flasks for cell culture expansion. Cell viability and number was assessed using the Countess II FL Automated Cell Counter (ThermoFisher Scientific, Waltham, MA, USA). For downstream analytics, cells were pelleted to create multiple aliquots (3 x 106 cells per aliquot) and stored at −80 °C until further analysis.

3. Co-transfection of m6A writers, readers and erasers

Gli36 EGFRvIII cells were co-transfected to simultaneously knock down 1) METTL3 and METTL14 (m6A writers), 2) YTHDF2 and IGF2BP2 (m6A readers), and 3) ALKBH5 and FTO (m6A erasers). Cells were plated on Day 0 before transfection: 175k cells/well cultured in Opti-MEM for 24h in 6-well plates. After 24h, cells were transfected with Lipofectamine RNAiMAX Reagent (ThermoFisher Scientific, Waltham, MA, USA) per manufacturer's instructions. Each individual siRNA mixture was prepared by diluting 3uL of 10uM siRNA in 150uL of Opti-MEM and the Lipofectamine RNAiMAX mixture was prepared by diluting 9uL of the reagent in 150uL of Opti-MEM. The two were mixed in a 1:1 ratio and incubated at room temperature for 5min. Following the incubation, 250uL of each respective siRNA-lipid complex were added to the wells in accordance with each cotransfection mix. The plates were gently rocked back and forth to mix and the cells incubated for 48h. On Day 3, cells were harvested from the plate through trypsinization and washed with PBS before RNA was extracted from the cells using the RNeasy Kit for RNA Purification (Qiagen, Hilden, Germany) per manufacturer's instructions. The concentration and purity of each RNA sample were evaluated using a NanoDrop One Spectrophotometer (Thermo Fisher Scientific, Waltham, MA, USA). Isolated RNA samples were stored in −80 °C prior to downstream analysis.

3.1. Mycoplasma contamination testing

Testing for mycoplasma contamination was performed using a commercial mycoplasma PCR kit (PCR Mycoplasma Detection kit; Applied Biological Materials Incorporated, BC, Canada). The testing was done at two stages of the workflow: (i) Day 3, end of 48h transfection period, and (ii) Day 7, prior to transfer of cells from T-75 flask to Nunc™ TripleFlask™.

3.2. Assessment of transfection efficiency

Quantification (percentage gene knockdown) and stability of transfection were assessed using quantitative polymerase chain reaction (qPCR) measurement of the target. To ensure stability of transfection, quantification was performed using cells collected from 6 well plate. Commercially available, pre-designed primers were purchased (ThermoFisher Scientific, Waltham, MA, USA) for ALKBH5, IGF2BP2, METTL3, FTO, YTHDF2 and METTL14. Isolated total RNA from transfected (KD, control) cells was reverse transcribed using SuperScript™ VILO™ cDNA Synthesis Kit (ThermoFisher Scientific, Waltham, MA, USA). The qPCR reaction was performed in the Applied Biosystems StepOnePlus Real-Time PCR (Thermo Fisher Scientific) in a final volume of 20 μl and was prepared using 10 μl of SYBR Green Master Mix (ThermoFisher Scientific), 1500 nM forward and reverse primers (each transfection condition and GAPDH) and water to 20uL. Each sample was run in duplicates. The data was analyzed by visualizing amplification

plots and comparing the Cycle threshold (Ct) values in knockdown (ALKBH5, IGF2BP2, METTL3, FTO, YTHDF2, METTL14) and control (scrambled siRNA) wells. Normalization was performed using GAPDH as a reference assay (ThermoFisher Scientific) to compute the ΔΔCt values for each knockdown condition. The percent knockdown for each transfection was computed using formula (1-2^(-ΔΔCt))*100. The replicate with the highest knockdown was used for downstream analysis.

Transfection efficiency was consistently high across knockdown conditions used for both sequencing and qPCR validation. For sequenced samples, efficiencies were 87.9% for ALKBH5 KD, 55.6% for IGF2BP2 KD, and 60.4% for METTL3 KD. Validation experiments showed comparable or higher efficiencies, including 87.4% (FTO KD), 73.5% (IGF2BP2 KD), 70.2% (YTHDF2 KD), 94.7% (ALKBH5 KD), 94.0% (METTL14 KD), and 81.2% (METTL3 KD). For the co-transfections, efficiencies ranged from 69.8 to 76.6% for readers KD (IGF2BP2, YTHDF2), 68.0–71.0% for writers KD (METTL3, METTL14), and 70.4–82.6% for erasers KD (ALKBH5, FTO), supporting robust and reproducible knockdown across all conditions (Supplementary Fig. 10c and d; Supplementary Table 1).

3.3. Primer design

Isoform-specific primers were designed using NCBI Primer-BLAST to selectively amplify individual transcript isoforms. Primers were designed to target exon–exon junctions or exonic regions unique to each isoform based on human transcript annotations, and in silico specificity was confirmed using BLAST against the human transcriptome to minimize off-target amplification. Primer pairs were selected to generate amplicons within an appropriate size range for quantitative PCR. Gene-level primers were obtained from Thermo Fisher Scientific as pre-validated assays. Primer sequences are provided in Supplementary Table 3.

3.4. qPCR quality control for validation experiments

For the validation experiments for the isoform switching analyses, we ran qPCRs for each sample with two technical replicates. The correlation value between the CT values for qPCR replicate 1 and replicate 2 was 98.9%, p-value <2.2e-16 (Supplementary Fig. 10a). The distribution of GAPDH values were stable across the KD, Naive, and Scrambled conditions (Supplementary Fig. 10b).

3.5. Statistical testing

Quantitative PCR data were analyzed using the ΔΔCt method with GAPDH as the reference gene. Ct values from qPCR technical replicates ($n = 2$) were averaged prior to downstream analysis. For each target gene or isoform, ΔCt values were calculated relative to GAPDH, and ΔΔCt values were computed relative to the naïve control condition. Statistical comparisons were performed on ΔΔCt values using unpaired, two-tailed Student's t-tests, comparing each knockdown condition to the naïve control within each experimental run (Supplementary Fig. 10e). Fold changes ($2^{-}\Delta\Delta Ct$) are presented for visualization purposes only. Statistical significance was defined as $p < 0.05$. All analyses were conducted in R (version 4.4.0).

3.6. Cellular RNA extraction and quantification

Total RNA was extracted from transfected cells using TRIzol lysis reagent (ThermoFisher Scientific, Waltham, MA, USA) per manufacturer's protocol. For each condition, 3 x 10^6 million cells were lysed using 3 ml TRIzol. The extracted RNA was then eluted in 50 μl of nuclease free water (Qiagen). Agilent RNA 6000 Pico Kit was used with Agilent Technologies 2100 Bioanalyzer to determine the concentration and RIN (RNA Integrity Number) value of the samples. RIN values ranged from 9.3 to 9.75 across all samples. Isolated RNA was stored at −80 °C prior to downstream analysis.

3.6.1. Cellular RNA (mRNA) enrichment

Following Cell RNA extraction, total RNA was selectively enriched for mRNA using RiboMinus™ Eukaryote Kit v2 (ThermoFisher Scientific, Waltham, MA, USA) per manufacturer's recommendations. This provides transcriptome isolation downstream sequencing by selectively depleting 5S, 5.8S, 18S, and 28S ribosomal RNA from total RNA. For high yield cell RNA, RiboMinus™ Eukaryote Kit v2 (Catalog ID: A15026) was used to maximize the mRNA enrichment and overall recovery.

3.7. RNA quality control steps

Different measures were integrated throughout the workflow for quantitative and qualitative analysis of cell RNA. Quantification of “isolated total RNA” and “mRNA post rRNA depletion” was performed using Bioanalyzer Agilent RNA 6000 Pico Kit. Overnight ethanol precipitation with 3 M sodium acetate at −20 °C was performed post RNA extraction and post rRNA depletion to prevent carry over inhibitors during library preparation.

3.8. Library preparation and sequencing

Direct RNA sequencing of cell-derived mRNA was performed using Oxford Nanopore Technologies (ONT) platforms. Libraries were prepared using the SQK-RNA002 (ONT) kit according to the manufacturer's protocol and sequenced on the MinION platform using R9.4.1 flow cells (FLO-MIN106D, ONT). No multiplexing was performed; each sample was sequenced individually for 24–72 h.

4. Data analysis

4.1. Preprocessing

Raw RNA sequencing reads from cells, generated using Oxford Nanopore Technologies (ONT), were basecalled from POD5 files using Dorado (v0.5) with default parameters. The decoder file “rna002_70bps_fast@v3” was employed to convert raw signal data into FASTQ format, optimized for RNA sequencing at 70 base pairs per second. Reads that passed Dorado's default quality filters were retained for downstream analysis. The basecalled reads were then aligned to the human transcriptome (GENCODE v45, GRCh38) using minimap2 (v2.17). All passing aligned reads were included in the analysis. The BAM files were sorted and indexed using Samtools (v1.10). The processed and indexed BAM files were then used for transcript quantification and subsequent analyses. Per condition, plots were computed to compare average read length vs. read quality (Supplementary Fig. 1). Non weighted histograms of read lengths after log transformation were also compared across all experimental conditions (Supplementary Fig. 2). Raw data is available on the Harvard Dataverse at this link: https://dataverse.harvard.edu/dataset.xhtml?persistentId=doi:10.7910/DVN/8TFC38.

4.2. Quantification

Transcript and gene quantification was performed using bambu (v3.11.1), which supports the quantification of both known and novel transcripts and genes, as well as full length transcripts from long-read RNA sequencing data. BAM files generated by minimap2 were used as input along with the GENCODE v45 GRCh38 genome and annotation files. Transcript expression levels were quantified for each sample, with both raw counts and counts per million (CPM) values calculated. Bambu was configured to detect novel transcript isoforms in addition to quantifying known transcripts. To ensure robust quantification, transcripts with zero counts were excluded from analysis. This filtering step

reduced the noise and ensured that low-abundance transcripts did not affect downstream analyses.

4.3. Differential expression analysis

Using DESeq2 (v1.48.1), differential gene expression (DGE) analysis was performed on the transcripts and gene counts between the control (Naive), Scrambled, and knockdown conditions (IGF2BP2, METTL3, ALKBH5 knockdowns (Supplementary Figs. 12 and 13). For each comparison, genes and transcripts with less than 1 count across all samples were filtered out, and remaining counts were normalized using DESeq's internal size factor estimation. Transcripts and genes with a fold change of at least 1.5 (log2fFC >0.58, log2FC < -0.58) and an adjusted p-value (Benjamini-Hochberg) less than 0.05 were considered significantly differentially expressed. EnhancedVolcano (v1.24) in R was used to visualize fold changes and statistical significance for each pairwise comparison. pheatmap (v1.0.12) was used to generate heatmaps of log2 fold changes for genes and transcripts corresponding to (i) known m6A regulators, (ii) RNA splicing, and (iii) RNA decay. For RNA splicing and RNA decay, unsupervised hierarchical clustering using Euclidean distance was applied to rows to identify shared expression profiles across conditions. Significant log2 fold changes (p-value <0.05) were denoted with asterisks.

4.4. Isoform usage analysis

Differential isoform usage analysis was performed in R using IsoformSwitchAnalyzeR38 (2.8.0). The aggregated isoform counts and abundances were input along with the human (GRCh38.p14) annotation and transcriptome files. Single isoform genes were filtered out during the prefilter() step since these genes cannot exhibit changes in isoform usage. Statistical analysis was performed with isoform SwitchTestDEXSeq() with parameters reduceToSwitchingGenes = TRUE, reduceFurtherToGenesWithConsequencePotential = TRUE, keepIsoformInAllConditions = FALSE. We required a difference in isoform proportions between classification groups of >0.1 and an FDR-adjusted p-value of <0.05 for significance. The functional consequences of the identified isoform switches were generated using the analyzeSwitchConsequences() function. This analysis identified changes in key functional domains such as coding potential, exon loss, domain loss, and isoform length where the difference in isoform proportions is greater than 0.4. Alternative splicing analysis was performed using the analyzeAlternativeSplicing() function, which identified and assessed the significance of specific events such as alternative 3' acceptor site (A3) gain or loss. Consequence plots were generated that show the fraction of significant isoform switches that have a specific consequence and its opposing consequence in each comparison.

4.5. Isoform switching analyses with scrambled condition

Isoform switching between scrambled siRNA and naïve cells was evaluated using IsoformSwitchAnalyzeR with isoformSwitchTestDEXSeq, applying the same filtering and statistical parameters used for the knockdown (KD) versus naïve comparisons. This analysis identified 618 switching isoforms across 403 genes (Supplementary Fig. 8a).

However, examination of the joint distribution of differential gene expression (log2 fold change) and differential isoform usage (dIF) revealed a systematic skew not observed in other contrasts (Supplementary Fig. 8b and 8c). Specifically, most genes identified as switching were upregulated in the naive condition, with larger dIF values corresponding to greater upregulation. In contrast, KD vs naive comparisons displayed approximately symmetric distributions of gene expression and isoform usage changes (Supplementary Fig. 8d and 8e).

Normalization diagnostics indicated substantial library size imbalance between scrambled (size factors: 0.27, 0.36, 0.82) and naïve samples (2.30, 2.51, 2.71), representing an approximately 10-fold range. Because sequencing depth was strongly confounded with condition in this comparison, DEXSeq normalization assumptions were violated, leading to skewed fold-change distributions and inflated differential isoform usage estimates consistent with depth-driven artifacts.

In KD versus naïve analyses, sequencing depth varied across multiple groups (size factors 0.31–2.23) rather than being exclusively associated with a single condition, and no systematic skewing was observed. Although alternative methods such as satuRn were considered, DEXSeq was selected due to its robustness in experiments with fewer than five replicates per condition, and a unified model including scrambled samples was not feasible given the number of surrogate variables relative to replicates.

For these reasons, scrambled versus naïve isoform switching results were not included in downstream biological interpretation.

4.6. Transcriptome-wide m6A-modified sites

RNA methylation analysis was conducted using m6anet (v2.1.0), a machine learning-based tool, to detect RNA modifications at single-nucleotide resolution. BAM files obtained from minimap2 were input to m6anet, along with the raw FAST5 files, FASTQ, and transcriptome files. The model was trained using the RNA004 direct RNA-Seq run using HEK293T cell line. As m6anet supports pooling over replicates, the replicates (n = 3) per condition were pooled prior to the inference step. The output of m6Anet includes predicted m6A sites with an associated modification probability, the transcriptomic position of each site, the corresponding DRACH motif (5-mer sequence context), and the estimated proportion of reads at each site predicted to be modified. Sites with a probability of modification greater than 0.9 were considered high confidence m6a sites and retained for downstream analysis. Post processing of m6a site predictions was conducted using a custom R package, m6AnetAnalyzer [22], to standardize and streamline downstream processes. Key metrics such as the distribution of modified sites, transcripts, and genes, the frequency of transcript biotypes, k-mer enrichment, and the length distribution of modified transcripts were computed and visualized.

4.7. Distribution of modified sites

m6AnetAnalyzer was used to calculate the lengths of the 5′ UTR, CDS, and 3′ UTR regions in order to analyze the distribution of m6A-modified sites across transcript regions. For each transcript, the coding sequence (CDS) length was determined by summing exon lengths, while the UTR lengths were calculated based on start and end coordinates. Transcripts with missing UTR annotations were assigned a length of zero for the missing regions. To visualize the distribution of m6A-modified sites across these regions, the transcript position of each modification site was compared with the UTR and CDS regions to determine if the site was located within the 5′ UTR, CDS, or 3′ UTR. The relative position within each region was calculated, and kernel density estimation (KDE) plots were generated to visualize the relative density of m6A sites across these transcript regions. Modifications grouped by transcript biotypes (protein-coding, nonsense mediated decay, retained intron) and methylation status were visualized.

4.8. Identification of hyper- and hypo-m6A methylated transcripts

To identify hyper- and hypo-m6A methylated transcripts, we first filtered for transcripts present in all knockdown conditions (ALKBH5, IGF2BP2, and METTL3) vs. Naive group. For these commonly modified transcripts, we calculated the average modification ratio for each site within each classification. Finally, to calculate the weighted modification ratio for these commonly modified transcripts, we summed the modification ratios of all sites within each transcript and divided by the transcript length. This approach ensured that transcripts with more

modified sites contributed proportionally while preventing length bias, allowing for a more accurate comparison of modification levels across transcripts of varying lengths. To identify hypermethylated and hypomethylated transcripts, we calculated the log2 fold change of the weighted modification ratio for each pairwise comparison (n = 7). A positive log2FC indicated that a transcript was hypermethylated in Naive (vs. ALK (vs. METTL3, IGF2BP2, Naive), IGF2BP2 (vs. METTLE3, Naive), or METTL3 (vs. Naive), while a negative log2FC indicated that a transcript was hypermethylated in (vs. Naive), METTL3 (vs. ALKBH5, IGF2BP2), Naive (vs. ALKBH5, IGF2BP2, METTLE3), or IGF2BP2 (vs. ALKBH5). ggplot2 (v3.5.2) in R was used to illustrate the different biotypes distribution in each cluster by plotting a stacked barchart for all pairwise comparisons.

4.9. Functional analysis of isoform switching and hyper- and hypo-m6A methylated genes

Functional analysis was performed using ClusterProfiler39 (4.14.6) for all Gene ontologies (Biological Process, Molecular Function, and Cellular Component) and KEGG pathways. The enrichGO function was applied for genes that were upregulated and had m6A modifications in each tumor classification. For each comparison, plots were generated that show the amount of differentially expressed genes associated with the top twenty pathways based on fold enrichment score. Heatmaps of differential gene expression and the associated m6a modifications were generated for selected enriched pathways (i.e. Apoptosis, MAPK Signaling, Oxidative Phosphorylation).

4.10. Gene Set Enrichment Analysis

Gene Set Enrichment Analysis was used to show pathways that are significantly associated within the selected gene list. Gene set enrichment analysis is used to determine if an inputted gene list is overly expressed in the enriched pathway.

4.11. External database validation

4.11.1. Validation of m6A regulator expression

GlioVis, an online visualization and analysis platform comprising approximately 6500 tumor samples across ~50 expression datasets, was used for external validation of m6A regulator expression. Expression levels of ALKBH5, IGF2BP2, and METTL3 were examined across glioma tumor grades. In addition, Kaplan–Meier survival analyses were conducted in GlioVis to assess associations between m6A regulator expression and overall survival. Patients were dichotomized into high- and low-expression groups using median gene expression as the cutoff. Survival curves were compared using the log-rank test, as implemented in GlioVis.

Findings were further validated using an independent human glioma tumor tissue cohort generated in our recent preprint study. This cohort included 6 astrocytomas, 2 oligodendrogliomas, and 6 glioblastoma (GBM) samples. Gene expression levels of ALKBH5, IGF2BP2, and METTL3 were examined across tumor types, and expression differences were assessed to determine consistency with trends observed in public datasets and cell line experiments.

4.11.2. Validation of isoform switching events

To validate isoform switching events identified in this study, we leveraged CanIsoNet, a disease-specific isoform interaction network that catalogs dominant transcripts in glioblastoma multiforme (GBM) (Project code: CNS-GBM; Dataset: PCAWG). Dominant GBM transcripts from CanIsoNet were overlapped with isoform switching events detected in our analysis based on matching transcript identifiers. This comparison was used to evaluate whether isoform switches identified in our dataset corresponded to dominant isoforms reported in independent GBM cohorts.

5. Results

5.1. Quality assessment and transcriptome-wide profiling of m6A regulator perturbations in glioma cells

To establish a controlled system for transcriptome-wide m6A profiling, we generated an *in vitro* glioma model with targeted knockdown (KD) of three core m6A regulators using small interfering RNAs (siRNAs): the reader IGF2BP2, the writer METTL3, and the eraser ALKBH5 (Fig. 1a; Methods). Untreated glioma cells (naïve), scrambled siRNA–treated cells were included as controls. In total, six experimental conditions were analyzed (see Methods). Direct RNA sequencing was performed in triplicate for each condition to enable assessment of reproducibility and technical variability (Fig. 1a).

Across all conditions, a total of 14.3 million reads were generated (Fig. 1b, Supplementary Figs. 1 and 2). Sequencing yield varied across conditions, with naïve producing the highest number of total reads, followed by knockdown, and scrambled glioma samples. A similar pattern was observed for mapped reads (Fig. 1c).

Across all conditions, protein-coding transcripts represented the dominant RNA biotype detected (Fig. 1d). Naïve glioma cells and METTL3 KD samples showed the highest proportion of protein-coding RNA, while IGF2BP2 KD, ALKBH5 KD and scrambled samples exhibited modestly lower proportions. Retained intron transcripts were present at low but variable levels across conditions, with slightly higher representation in IGF2BP2 and ALKBH5 KD samples compared with naïve glioma cells (Fig. 1d). Overall, global RNA biotype composition was largely preserved across perturbations.

Principal component analysis (PCA) was used to assess transcriptome-wide variance across samples (Fig. 1e). In comparisons among glioma-derived conditions, replicates generally clustered by condition, supporting reproducibility, although increased dispersion was observed for IGF2BP2 KD and scrambled, consistent with expected technical variability in direct RNA nanopore sequencing (Fig. 1e).

Analysis of read length distributions further demonstrated condition-dependent differences in transcript representation (Fig. 1f). Scrambled controls showed relatively higher proportions of shorter transcripts (≤500 bp), whereas naïve glioma and METTL3 KD samples were enriched for longer transcripts (501–5000 bp). IGF2BP2 KD and ALKBH5 KD samples displayed intermediate distributions.

Collectively, these analyses establish robust, transcriptome-wide direct RNA sequencing across perturbations of m6A regulatory machinery, with preserved global RNA composition and reproducible condition-level structure despite variability in sequencing yield. This dataset provides a foundation for downstream analyses of m6A architecture, transcript modification patterns, and isoform-level regulation.

5.2. Transcriptome wide mapping of m6A in naive glioma cells and m6A regulator knockdowns

We next characterized the distribution and abundance of m6A modifications to assess how perturbation of m6A regulatory machinery influences the epitranscriptomic landscape. m6A sites were predicted using m6Anet (v2.1.0), a machine learning–based framework optimized for long-read direct RNA sequencing (see Methods). We quantified the relative abundance of modified sites, transcripts, and genes across all conditions.

Naïve glioma cells displayed a higher burden of m6A, with 2.0% of sites, 23.4% of transcripts, and 30.2% of genes modified (Fig. 2a). All knockdown and scrambled conditions showed further reductions in detectable m6A relative to naïve glioma cells. Among the knockdowns, IGF2BP2 and METTL3 showed intermediate levels, while ALKBH5 exhibited the lowest prevalence of m6A-modified sites and transcripts, likely due to differences in sequencing in addition to the underlying biology of the perturbed regulator (Fig. 1b–c, 2a).

Despite differences in overall m6A abundance, the distribution of

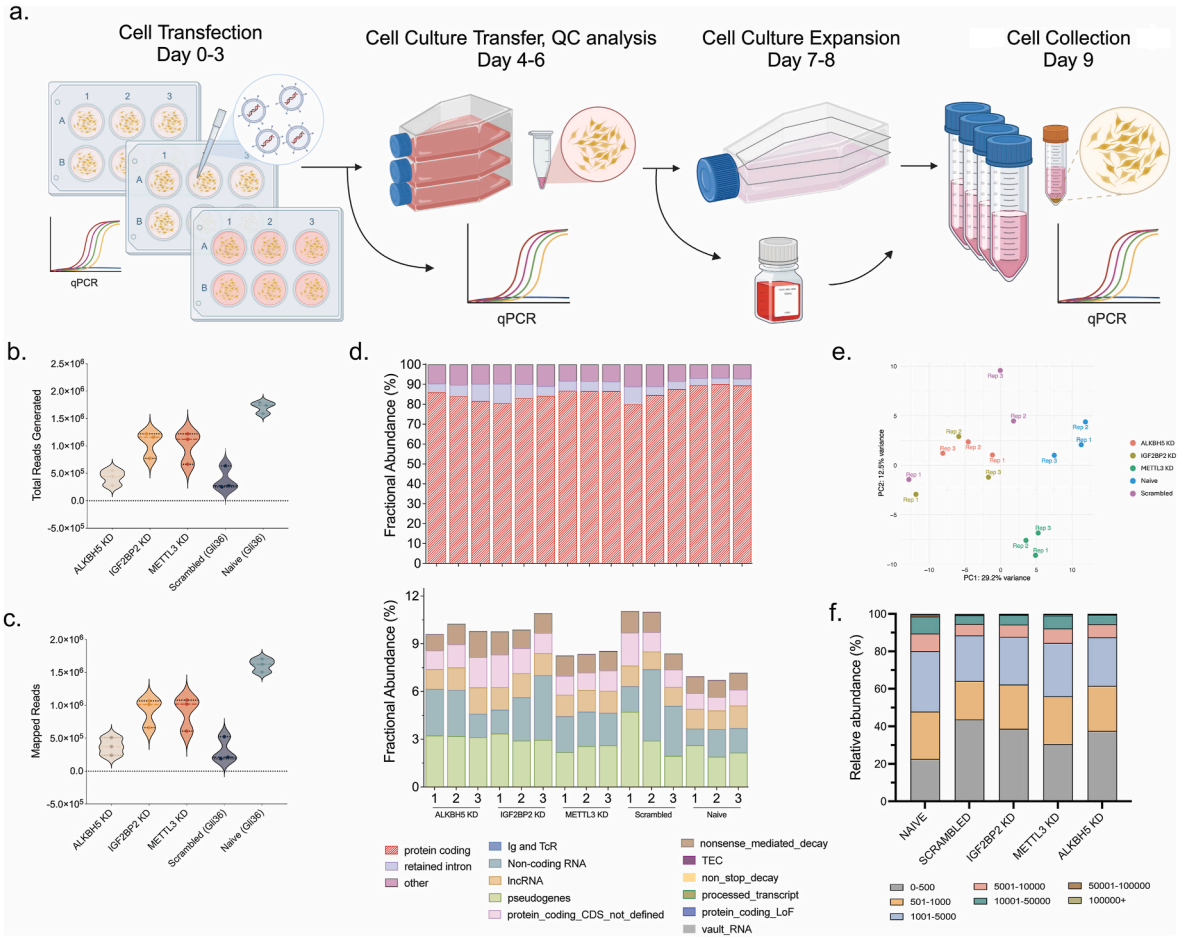

Fig. 1. Transcriptome wide profiling of m6A in Gli36 glioma cell line. (a) Schematic depicting cell transfection with silencer RNA (siRNA) to achieve knockdown (KD) of key m6A regulators: IGF2BP2 (reader), METTL3 (writer), ALKBH5 (eraser). RNA isolated from control (naïve, scrambled siRNA) and KD cells on day 9 sequenced using Nanopore direct RNA sequencing platform. Three technical replicates were sequenced per condition. (b) Total and (c) Mapped reads across the three replicates of cell RNA sequenced from glioma and KD conditions. (d) Distribution analysis of the detected RNA biotypes from control and KD conditions. (e) Assessment of variance in the cell RNA detected transcripts using principal component analysis (PCA). (f) Distribution analysis of the detected RNA biotypes from control and KD conditions.

m6A-modified RNA biotypes was largely conserved across conditions. Protein-coding transcripts constituted the majority of m6A-marked RNA (70.5–79.0%), followed by transcripts subject to nonsense-mediated decay and retained intron–containing transcripts (Fig. 2b). No major shifts in RNA class composition were observed between naïve glioma cells, scrambled controls, or knockdown conditions.

We next examined the positional distribution of m6A sites along transcripts (Fig. 2c). Naïve glioma cells and scrambled controls showed relatively high m6A density in the proximal site of 3' UTR and within coding sequence (CDS) regions. Comparison of knockdown conditions to naïve glioma cells revealed a consistent reduction in CDS-associated m6A and relative enrichment toward the 3′UTR, with the most pronounced shift observed in ALKBH5 KD cells (Fig. 2c). These patterns suggest that perturbation of m6A regulatory machinery, likely influences regional m6A bias.

Analysis of site multiplicity demonstrated that most m6A-modified transcripts contained a single m6A site across all conditions (Fig. 2d). Naive showed multiple m6A sites, with up to 13 sites detected on individual transcripts. In contrast, scrambled and knockdown conditions predominantly harbored transcripts with fewer modification sites.

Because transcript structure can influence m6A deposition [23], we assessed m6A prevalence across transcript length categories (Fig. 2e). Across all conditions, m6A modifications were most frequently detected in transcripts ranging from 1000 to 5000 nucleotides, while shorter transcripts (≤500 bp) were less likely modified despite their abundance. ALKBH5 KD samples showed modest enrichment of m6A-modified transcripts in the 500–1000 bp range relative to naïve glioma cells, whereas longer transcripts (>5000 bp) were infrequently methylated across all groups (Fig. 2e). CDS and 3′UTR length comparisons revealed a pronounced shift in ALKBH5 KD cells, with shorter and less dense CDS regions, while 3′UTR lengths remained largely unchanged (Supplementary Fig. 3a).

To further contextualize regional m6A architecture, we examined transcript-length–stratified positional density profiles in KD and naïve glioma cells (Fig. 2f). Naïve glioma cells and KD conditions exhibited similar junctional peaks but reduced m6A density across the distal 3′UTR (Fig. 2f; Supplementary Fig. 3b). These differences highlight cell-type–specific m6A distribution while preserving canonical positional features. Chromosomal distribution analyses revealed broadly similar patterns of m6A-modified genes across conditions and are presented in Supplementary Fig. 3c.

Together, these analyses describe consistent differences in m6A abundance and position across naïve glioma cells, and m6A regulator knockdown conditions, providing a framework for subsequent analyses of isoform-level and transcript-specific regulation.

5.3. Integration of m6A methylation and gene expression across m6A regulator knockdowns

To investigate how changes in m6A deposition relate to

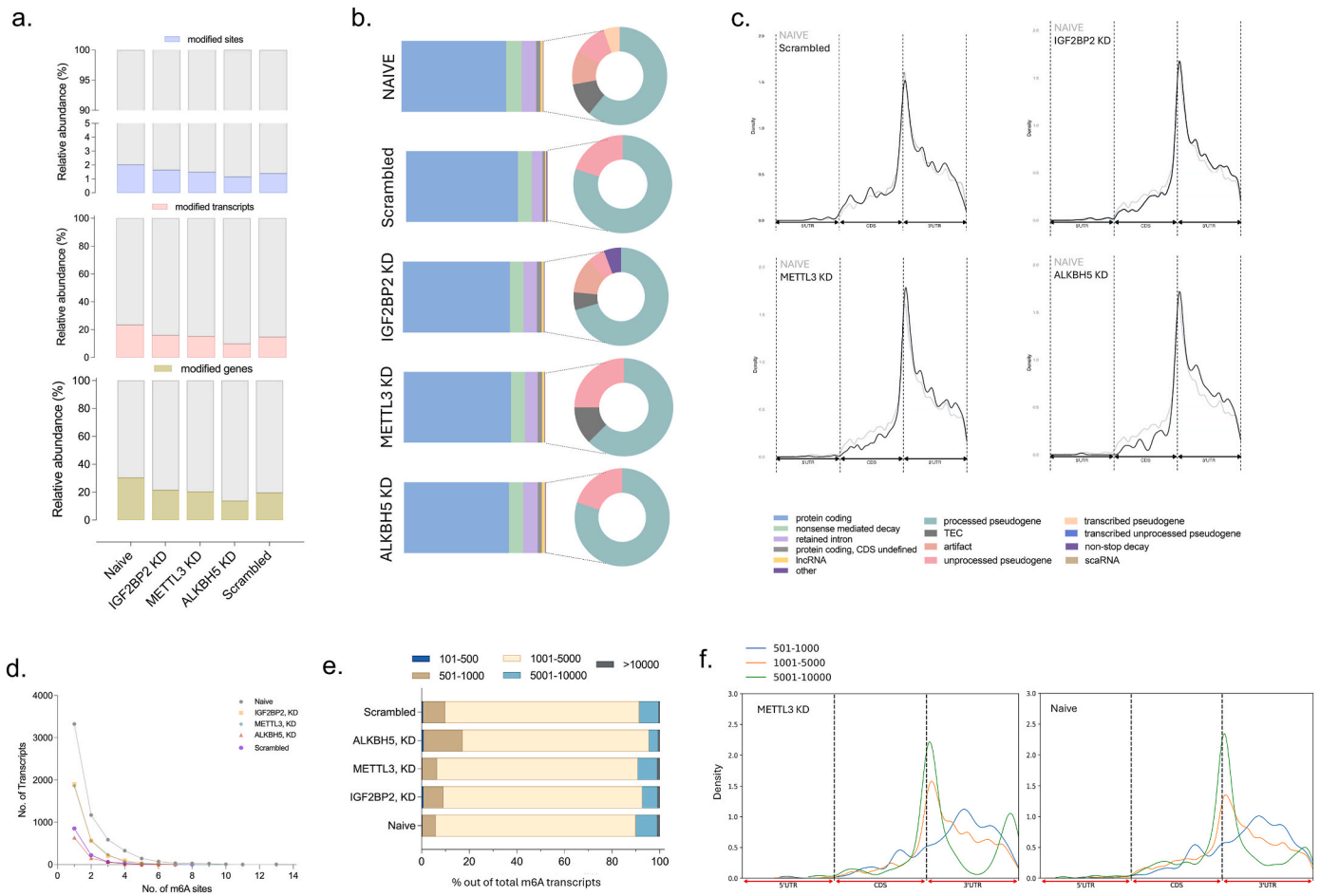

Fig. 2. Quantification of m6A modified RNA biotypes and transcript distribution. (a) Bar chart summarizing the relative abundance of m6A modified sites, transcripts, and genes for ALKBH5 KD, IGF2BP2 KD, METTL3 KD, scrambled siRNA, and naïve conditions. (b) Pie chart depicting the m6a modified transcript biotype distribution in each condition (n = 6). (c) KDE distribution of localization of m6A modified sites in the 5′UTR, CDS, and 3′UTR transcript regions in each KD condition (n = 3) and Scrambled (dark gray) in comparison to Naïve (gray). (d) Distribution of transcripts by number of m6A sites across experimental conditions, The y-axis indicates the number of transcripts, and the x-axis shows the number of m6A sites per transcript. (e) Stacked bar chart demonstrating the relative abundance of m6A modified RNA fragment length in each condition. (f) Density plots of m6A distribution along the transcript region, stratified by RNA length.

transcriptional output, we focused on transcripts commonly modified across naïve and knockdown (KD) glioma cells. Intersection analysis identified 719 m6A sites corresponding to 578 transcripts and 244 genes shared among ALKBH5 KD, IGF2BP2 KD, METTL3 KD, and naïve conditions, which were then retained for downstream analyses (Fig. 3a; Supplementary Fig. 3d).

For each transcript, m6A methylation was quantified using a weighted modification ratio that accounts for both site-level modification probability and transcript length (see Methods). Differential methylation was assessed in three pairwise comparisons: ALKBH5 KD vs naïve, IGF2BP2 KD vs naïve, and METTL3 KD vs naïve, and correlated with gene-level expression changes (Fig. 3b; Supplementary Fig. 4a).

Across all comparisons, most commonly modified transcripts were hypermethylated in the naïve condition relative to knockdown states (Fig. 3b). The magnitude of methylation loss varied by regulator, with ALKBH5 KD showing the most pronounced reduction ($\log2FC \leq -4$), likely reflective of overall cellular stress, followed by IGF2BP2 KD and METTL3 KD ($\log2FC \leq -3$). Differential gene expression patterns were regulator dependent: ALKBH5 KD vs naïve showed a predominance of upregulated genes in the KD condition, METTL3 KD vs naïve showed slightly more genes upregulated in naïve cells, and IGF2BP2 KD vs naïve displayed a more balanced distribution of up- and down-regulated genes (Fig. 3b).

We next examined whether transcript region–specific m6A localization contributed to these patterns. Among commonly modified transcripts, regional enrichment broadly mirrored the global m6A landscape (Supplementary Fig. 4b). In protein-coding transcripts, m6A sites were preferentially localized to the CDS in the naïve condition, whereas KD conditions exhibited relatively greater 3′UTR enrichment. In nonsense-mediated decay transcripts, m6A sites were consistently enriched toward the distal 3′UTR across all conditions.

Hypermethylated transcripts in both the KD and naïve conditions contained more m6A sites in the 3′UTR than in the CDS (Fig. 3c). Similar regional m6A distributions were observed when transcripts were further stratified by methylation status and expression change (Supplementary Fig. 4c–e). Specifically, transcripts that were both upregulated and hypermethylated in either the naïve or KD conditions were more often modified in the 3′UTR (Supplementary Fig. 4d and e). Notably, in the ALKBH5 KD versus naïve comparison, transcripts hypermethylated in the naïve condition but associated with downregulated gene expression showed a higher proportion of CDS methylation (Supplementary Fig. 4d and e).

To place these observations in functional context, gene set enrichment analysis was performed on commonly modified genes (Fig. 3d; Supplementary Fig. 4f; Supplementary Fig. 5). Integration of differential methylation and gene expression revealed regulator-specific pathway patterns. In RNA-binding pathways, ALKBH5 KD was characterized by marked hypomethylation, with increased expression of PUF60 and

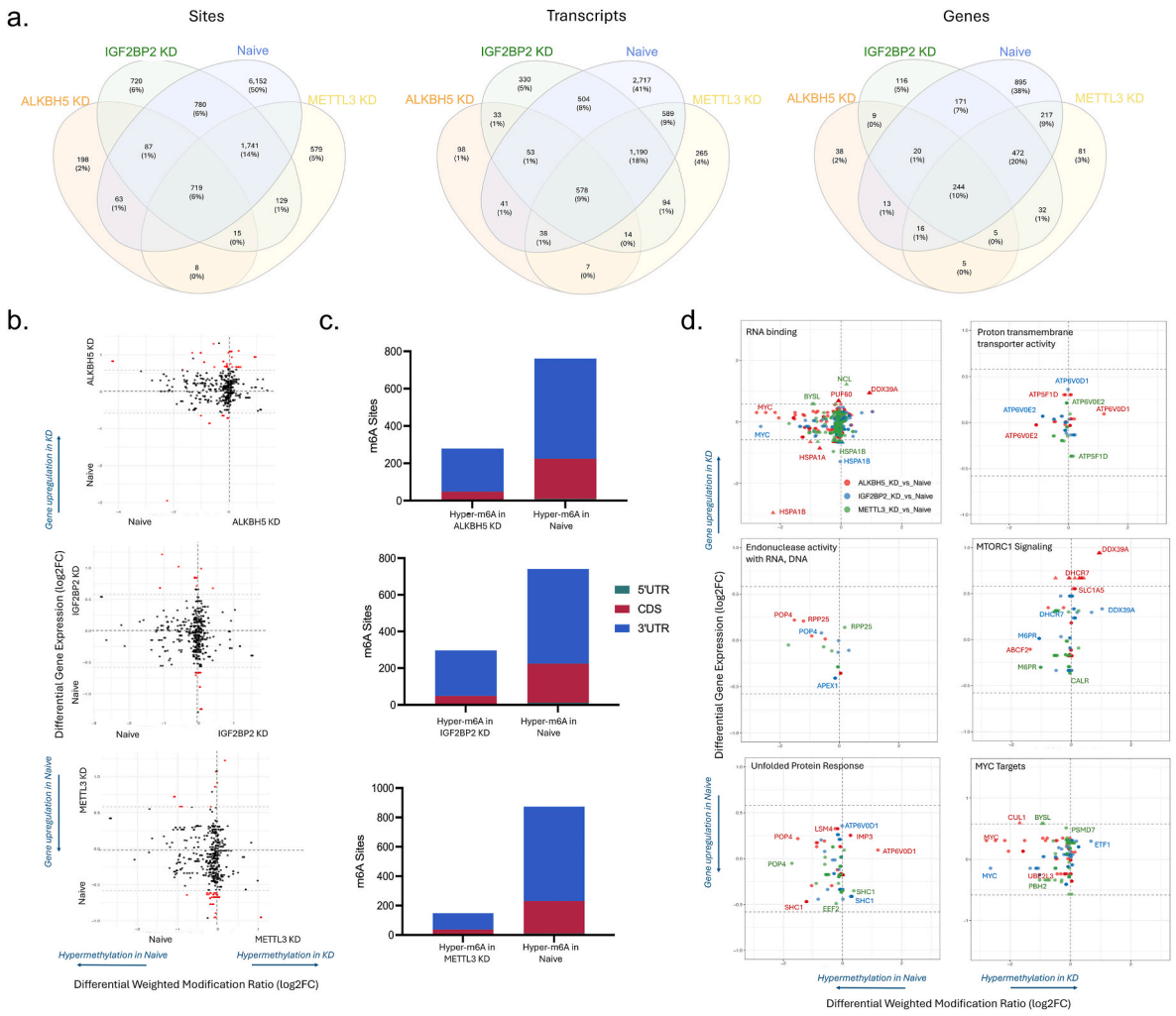

Fig. 3. Integration of m6A methylation, gene expression, transcript regions, and pathway-level changes across m6A regulator knockdowns. (a) Venn diagram of the common and unique m6A modified sites, tra=nscripts, and genes across the four conditions, respectively. N = 578 transcripts are used for downstream analysis. (b) Scatter plots illustrating the m6A methylation vs. differential gene expression of commonly m6A modified genes. The x-axis represents the log2 fold change (FC) in m6A methylation levels, while the y-axis denotes the log2 FC of differentially expressed genes (DGEs). DGEs with Log2 FC > 0.58 or < −0.58 and p-value <0.05 are highlighted in red, while non-significant ones are shown in gray. (c) Stacked bar graphs showing the proportional distribution of m6A sites across transcript regions (3′UTR and CDS) for hypermethylated transcripts within each comparison. (d) Scatter plots of selected pathways containing commonly m6A modified genes and displaying differential methylation and gene expression levels between in each knockdown condition compared to naïve.

DDX39A and reduced expression of HSPA1A/B relative to naïve cells. MYC was consistently hypomethylated in ALKBH5 and IGF2BP2 KD but did not exhibit corresponding expression changes. Genes involved in RNA/DNA endonuclease activity (e.g., POP4, RPP25) were broadly hypomethylated in ALKBH5 and IGF2BP2 KD, whereas RPP25 was hypermethylated in METTL3 KD.

Additional pathway-specific differences were observed in proton transmembrane transport, unfolded protein response, and mTORC1 signaling, with overlapping but non-identical methylation patterns across knockdowns (Fig. 3d). In several cases, differential gene expression occurred in the absence of detectable methylation changes, indicating that altered m6A deposition was not uniformly predictive of transcriptional output across pathways.

5.4. *Unique m6A methylation landscapes in naive glioma cells, and regulator knockdowns*

We next analyzed m6A sites, transcripts, and genes unique to each condition, focusing primarily on naive glioma cells relative to each KD. Naive glioma cells harbored the highest number of unique m6A sites, transcripts and genes (6148 sites, 3653 transcripts, 1520 genes), followed by IGF2BP2 KD (720 sites, 682 transcripts, 355 genes), METTL3 KD (579 sites, 536 transcripts, 281 genes), and ALKBH5 KD (200 sites, 194 transcripts, 104 genes; Fig. 4a).

Biotype distributions of uniquely m6A-modified transcripts were broadly similar across conditions (Supplementary Fig. 6a). Protein-coding transcripts predominated in all groups, with slightly higher proportions in ALKBH5 KD (77.3%) and IGF2BP2 KD (75.1%) compared with naïve (73.3%) and METTL3 KD (73.1%). Among non-coding RNA categories, IGF2BP2 KD and naive showed slightly higher proportions of m6A-modified lncRNAs (1.8%; 1.9%).

K-mer analysis of unique m6A sites revealed motif shifts across conditions (Supplementary Fig. 6f). GGACT was most enriched in naïve cells (35.7%). In KD conditions GGACT was reduced while GAACT became more prevalent, reaching 34.4% in METTL3 KD, 33.1% in IGF2BP2 KD and 35.0% in ALKBH5 KD. GGACT depletion was most pronounced in IGF2BP2 KD (19.7%) and ALKBH5 KD (22.0%), whereas METTL3 KD retained a relatively higher proportion (28.3%). TGACT was most enriched in IGF2BP2 KD (17.5%), while AGACT was more prevalent in naïve cells (11.9%) than in ALKBH5 KD (9.5%), METTL3 KD (7.6%), or IGF2BP2 KD (6.0%; Supplementary Fig. 6b).

Transcriptomic regional mapping revealed condition specific

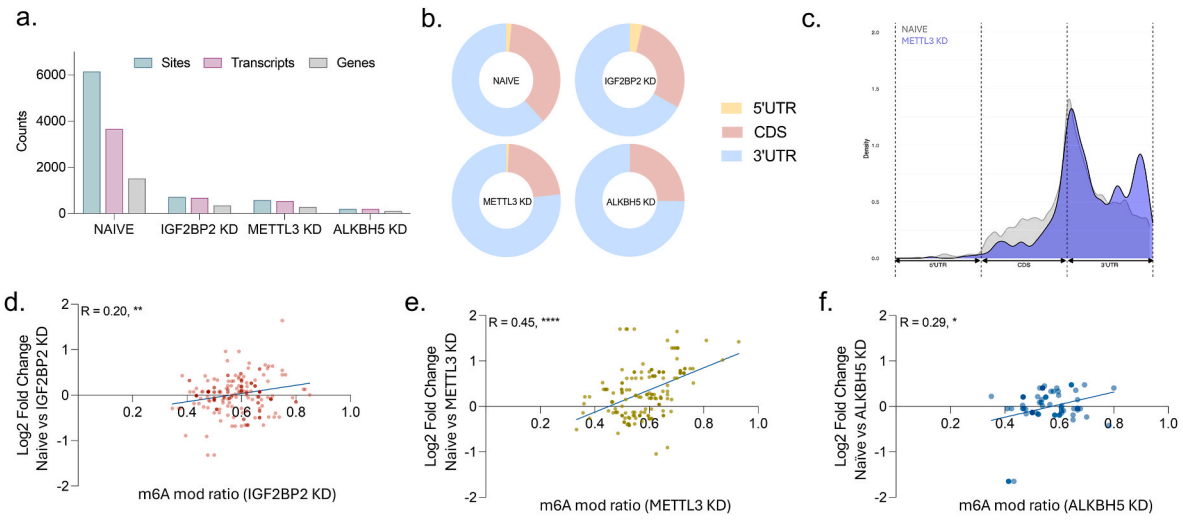

Fig. 4. Quantification of unique m6A modified sites, transcripts, and genes. (a) Grouped bar chart displaying the number of unique m6A modified sites, transcripts, and genes in each KD cell and the naïve condition. (b) Pie charts representing the proportion of 5′UTR, CDS, and 3′UTR in uniquely modified m6A transcripts for each KD condition (n = 3) and the naïve condition. (c) KDE plots showing the transcript region density in METTL3 knockdown (blue) in comparison to naïve (gray). (d-f) Scatter plots of the m6A modified ratio (x-axis) against the log2 fold change to showcase the correlation between methylation and gene expression for KD conditions vs Naïve. Red represents IGF2BP2 KD, yellow represents METTL3 knockdown, and blue represents ALKBH5 knockdown.

patterns of m6A localization (Fig. 4b and c; Supplementary Fig. 6c). Across the glioma comparisons, 5′UTR modifications were slightly higher in IGF2BP2 KD (3.7%), a 2.3-fold higher enrichment compared to naive glioma cells (1.6%) (Fig. 4b; Supplementary Fig. 6c). Consistent with the common site analysis, naive cells showed the highest CDS (36.4%) and lowest 3′UTR (62.0%) methylation, yielding the highest CDS:3′UTR ratio (0.59). All KD conditions showed reduced CDS methylation and increased 3′UTR methylation (Fig. 4b and c; Supplementary Fig. 6c). All KD conditions showed reduced CDS methylation and increased 3′UTR methylation: ALKBH5 KD (CDS: 25.3%, 3′UTR: 74.7%), METTL3 KD (22.4%, 76.8%), and IGF2BP2 KD (29.4%, 67.0%). Accordingly, CDS:3′UTR ratios were lower in all KD conditions, with the lowest ratio observed in METTL3 KD (0.29), followed by ALKBH5 KD (0.33) and IGF2BP2 KD (0.44; Fig. 4b and c; Supplementary Fig. 6c).

Chromosomal distribution of all detected m6A sites was similar across conditions. However, analysis restricted to uniquely modified sites revealed more distinct chromosomal enrichment patterns in KD cells (Supplementary Fig. 6d), including a tendency of higher m6A sites on chromosomes 1, 11, 17 and 19. Furthermore, chromosomes 4, 13, 18 and 21 consistently exhibited a lower number of m6A sites across all conditions (Supplementary Fig. 6d).

To determine whether these unique m6A changes were associated with transcriptional output, we correlated the weighted modification ratio with the corresponding gene expression levels (Fig. 4d–f; Supplementary Fig. 6e–g). In all KD conditions, uniquely modified transcripts showed a slightly positive correlation with gene expression relative to naive cells (Fig. 4d–f). This association was strongest in METTL3 KD (R = 0.45), followed by ALKBH5 KD (R = 0.29) and IGF2BP2 KD (R = 0.20), with all correlations reaching statistical significance.

5.5. Isoform switching and structural consequences of m6A regulator knockdown

Given the reported links between m6A regulators and RNA processing, we next examined whether knockdown of m6A regulators was associated with altered isoform usage using IsoformSwitchAnalyzeR [20] (see Methods). Isoform switching analysis revealed widespread, statistically significant changes across all conditions. Among knockdown (KD) conditions relative to naïve cells, ALKBH5 KD showed the highest number of isoform switches (1,364), followed by IGF2BP2 KD (821) and METTL3 KD (459; Fig. 5a; Supplementary Fig. 7a–b). The scrambled siRNA control was analyzed relative to naïve cells; however, because it showed an atypical distribution of differential gene expression and isoform usage that differed from both naïve and KD profiles (see Methods), it was excluded from primary comparisons and it is shown in Supplementary Fig. 8a–c for reference.

Across all conditions, 55.0% to 62.3% of high-usage isoforms were protein coding. Differences were more apparent among non-protein-coding isoforms, particularly retained intron and nonsense-mediated decay (NMD) transcripts. ALKBH5 KD cells showed a markedly higher proportion of high-usage NMD transcripts (27.4%), approximately 5-fold greater than other KD conditions (Fig. 5b). In contrast, retained intron isoforms were enriched in IGF2BP2 KD, METTL3 KD (IGF2BP2 KD: 32.5%, METTL3 KD: 26.7%), substantially exceeding the level observed in ALKBH5 KD (7.1%; Fig. 5b).

We next compared gene- and isoform-level log2 fold changes for high-usage isoforms in each KD condition relative to naïve cells (Supplementary Fig. 8d). High-usage isoforms were consistently upregulated within their respective KD conditions, whereas gene-level expression changes were more heterogeneous, with both up- and downregulation observed. These patterns indicate that differences in isoform usage were not uniformly reflected at the bulk gene-expression level and were often accompanied by increased representation of non-coding or decay-associated isoforms.

Structural consequence analysis further showed recurrent transcript-level changes across KD versus naïve comparisons (Fig. 5c). Consequences shared across all three KD conditions included complete open reading frame (ORF) loss, domain loss, exon loss, and shorter ORFs. NMD-sensitive isoforms were detected only in ALKBH5 KD cells (Fig. 5c). Additional consequences shared between IGF2BP2 KD and ALKBH5 KD included longer 5′UTRs, domain length loss, and increased usage of noncoding transcripts (Fig. 5c). Across all KD conditions, alternative splicing analysis showed broad changes relative to naïve cells, including intron retention, gain of alternative transcription start sites (ATSS), gain of alternative transcription termination sites (ATTS), and increased usage of alternative 5′ and 3′ splice sites (A5 and A3 gain; Supplementary Fig. 8e). Gene ontology analysis of genes associated with selected structural alterations is shown in Supplementary Fig. 9.

To further examine selected isoform switching events, we performed quantitative PCR (qPCR) on candidate genes and isoforms in KD conditions relative to naïve cells. Candidate isoforms were selected based on consistent increased usage across KDs and the presence of at least one

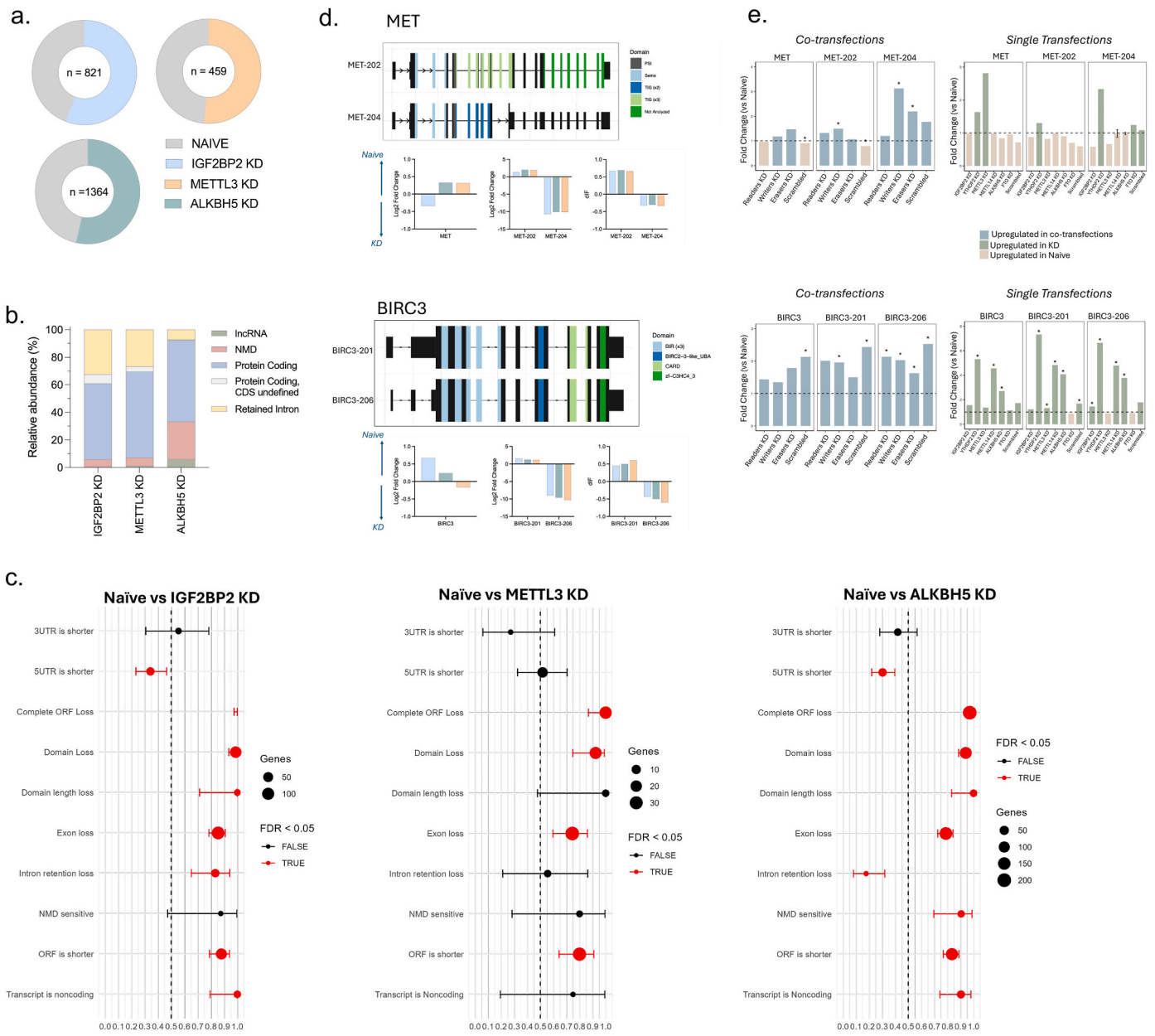

Fig. 5. Quantification of isoform switching events and its correlation to gene and isoform expression. (a) Pie chart quantifying the isoforms switches occurring between each KD condition compared to naïve condition. (b) Stacked bar chart indicating the biotype distribution of isoforms that are used more in KDs compared to naïve. (c) Isoform switch consequence plots that highlight the effect an isoform causes for the knockdown conditions. The x-axis depicts the ratio of number of genes with the specific consequence over the total number of genes effected by that consequence with the y-axis specifying the consequence. (d) Isoform switching of MET (top) and BIRC3 (bottom) in KD versus naïve glioma cells, with gene log2 fold change, isoform log2 fold change, and differential isoform usage (dIF) shown for each transcript. (e) qPCR fold changes for MET, BIRC3, and selected switching isoforms in single and co-transfection knockdowns relative to naïve controls, with scrambled serving as a control condition.

predicted functional consequence (Supplementary Tables 2 and 3). Ct values were normalized to GAPDH, and relative expression was calculated using the ΔΔCt method with statistical testing against naïve controls (see Methods and Supplementary Fig. 10)

Long-read sequencing analysis revealed little overall difference in MET gene expression between KD and naïve conditions, but isoform usage differed significantly. MET-204 was preferentially expressed in KD cells, whereas MET-202 predominated in naïve cells (Fig. 5d). The MET-204 switch was associated with predicted structural features including domain and exon loss, increased NMD sensitivity, a shorter ORF, and a longer 3′UTR. Similarly, qPCR analysis showed minimal differences for MET and its isoforms in single knockdowns, whereas co-transfections showed increased expression of MET-204 in reader (IGF2BP2, YTHDF2; fold change = 3.1) and eraser (FTO, ALKBH5; fold change = 2.2) knockdowns relative to naïve cells, with a smaller increase observed for MET-202 (fold change = 1.5; Fig. 5e)

The BIRC3 gene showed a similar pattern based on sequencing, with BIRC3-201 enriched in naïve cells and BIRC3-206 preferentially used in KD conditions (Fig. 5d). Increased usage of BIRC3-206 was associated with a shorter 5′UTR, exon gain, and reduced intron retention. qPCR, on the other hand, showed upregulation of BIRC3 and both isoforms in several single knockdowns, including YTHDF2, METTL14, and ALKBH5. In co-transfection experiments, total BIRC3 expression showed no significant gene-level change, whereas isoform-specific differences remained evident: BIRC3-201 was elevated primarily in writer knockdowns, while BIRC3-206 was increased across reader, writer, and eraser

knockdowns (Fig. 5e).

Together, these analyses show that m6A regulator knockdown was accompanied by broad shifts in isoform usage and predicted transcript structure, often in the absence of concordant gene-level expression changes.

5.6. Expression dynamics of m6A regulators, splicing factors, and decay machinery

We next examined expression changes in m6A regulators, their isoforms, and selected splicing and RNA decay factors across KD, naïve, and scrambled comparisons (Fig. 6). ALKBH5 was overall reduced in ALKBH5 KD comparisons, with ALKBH5-201 reaching statistical significance, highlighting differences in isoform vs gene expression. IGF2BP3 and IGF2BP3-201 were consistently downregulated in KD versus naïve comparisons, while IGF2BP2 and IGF2BP2-202 were increased in KD versus naïve cells. WTAP and several WTAP isoforms were elevated in naïve cells compared to KD conditions, whereas YTHDF2 and YTHDF2-208 showed their strongest increase in METTL3 KD versus naïve cells (Fig. 6a). Among splicing and decay factors, CNOT1 and DCP2 were consistently increased and EXOSC3 decreased across KD versus naïve comparisons (Fig. 6b). Matched analyses of gene expression together with transcript-level m6A weighted modification ratios across selected pathways are shown in Supplementary Figs. 11 and 12 and indicate that expression changes were not uniformly accompanied by parallel changes in m6A levels. Additional comparison-specific differential expression analyses are shown in Supplementary Figs. 13 and 14. Overall, these data indicate that m6A regulator perturbation is associated with broader shifts in the expression of RNA regulatory genes, with variable correspondence to transcript-level m6A changes.

5.7. Cross-dataset validation of m6A regulator expression and isoform usage in glioma

To examine m6A regulator expression in clinical glioma datasets, we queried GlioVis [24], which contains over 6500 primary brain tumor samples. ALKBH5 expression was highest in glioblastoma (GBM; $n = 225$, mean $\log2 = 4.79 \pm 0.96$), followed by astrocytoma ($n = 120$, mean $= 4.72 \pm 0.78$), and lowest in oligodendroglioma subtypes (Fig. 7a). IGF2BP2 expression was similarly enriched in GBM (mean $= 1.40 \pm 1.54$) and reduced in oligodendroglioma (Fig. 7a). In contrast, METTL3 expression was high in astrocytoma (mean $= 4.77 \pm 0.80$), with comparatively lower expression in GBM (Fig. 7a).

We next examined expression in our institutional glioma cohort ($n = 14$; Fig. 7b). Consistent with TCGA-based findings, IGF2BP2 expression was highest in GBM samples, whereas ALKBH5 showed greater variability but remained elevated across tumor grades. METTL3 expression was highest in astrocytoma, followed by GBM and oligodendroglioma, supporting concordance between our cell-line models and clinical datasets.

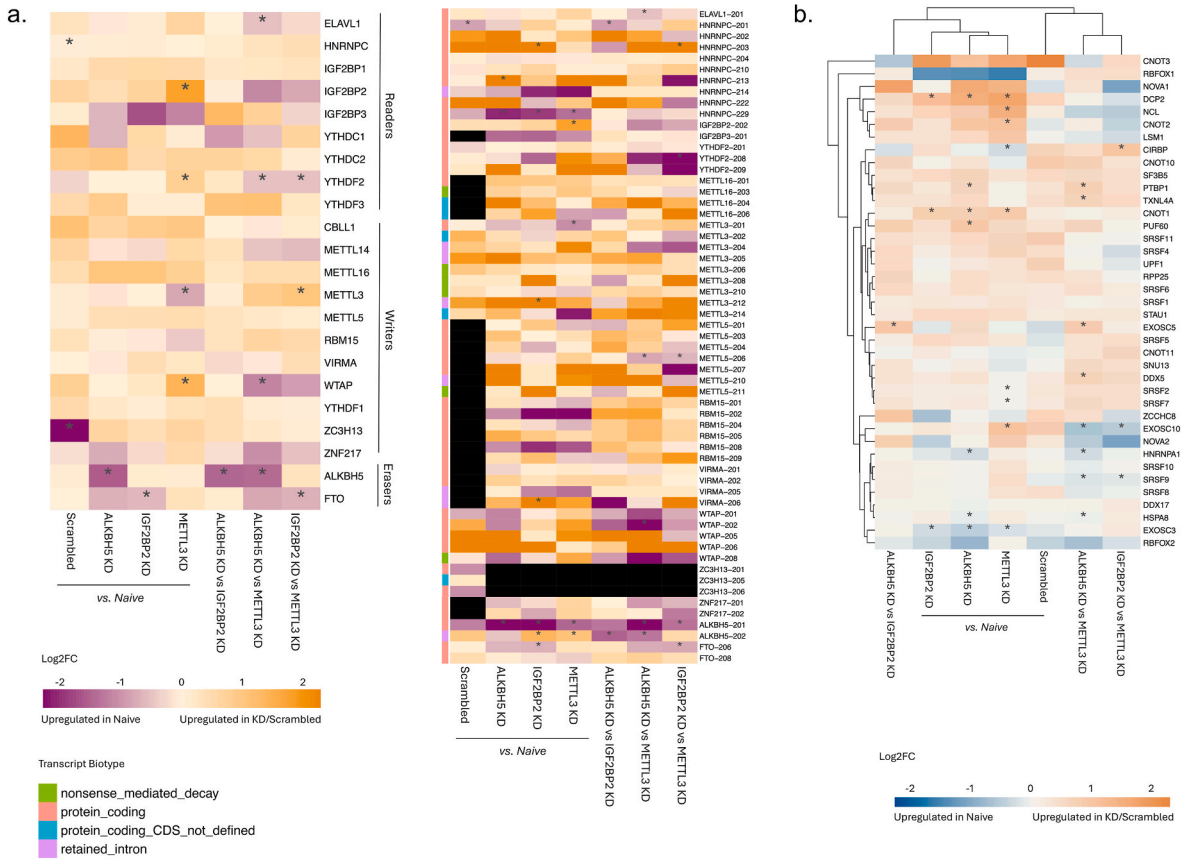

Fig. 6. Distribution analysis of m6A regulators, RNA splicing and decay factors across naïve and m6A regulator knockdowns. (a) Heatmaps summarizing the differential gene (left) and transcript (right) expression for m6A regulators. Each row represents a specific m6A RNA regulator gene/transcript and the columns represent the log2 fold change of expression for the eight pairwise comparisons. Orange indicates gene/transcript upregulation in the KD/Scrambled condition and purple indicates upregulation in the Naïve condition. Significant differential expression is indicated with a star and transcript biotypes are provided in the row annotations. (b) Heatmap depicting RNA splicing and decay factors in relation with gene expression. For KD/Scrambled conditions vs Naïve, orange indicates gene/transcript upregulation in the KD condition and blue indicates upregulation in the Naïve condition. Genes with significant changes in expression are highlighted with a star.

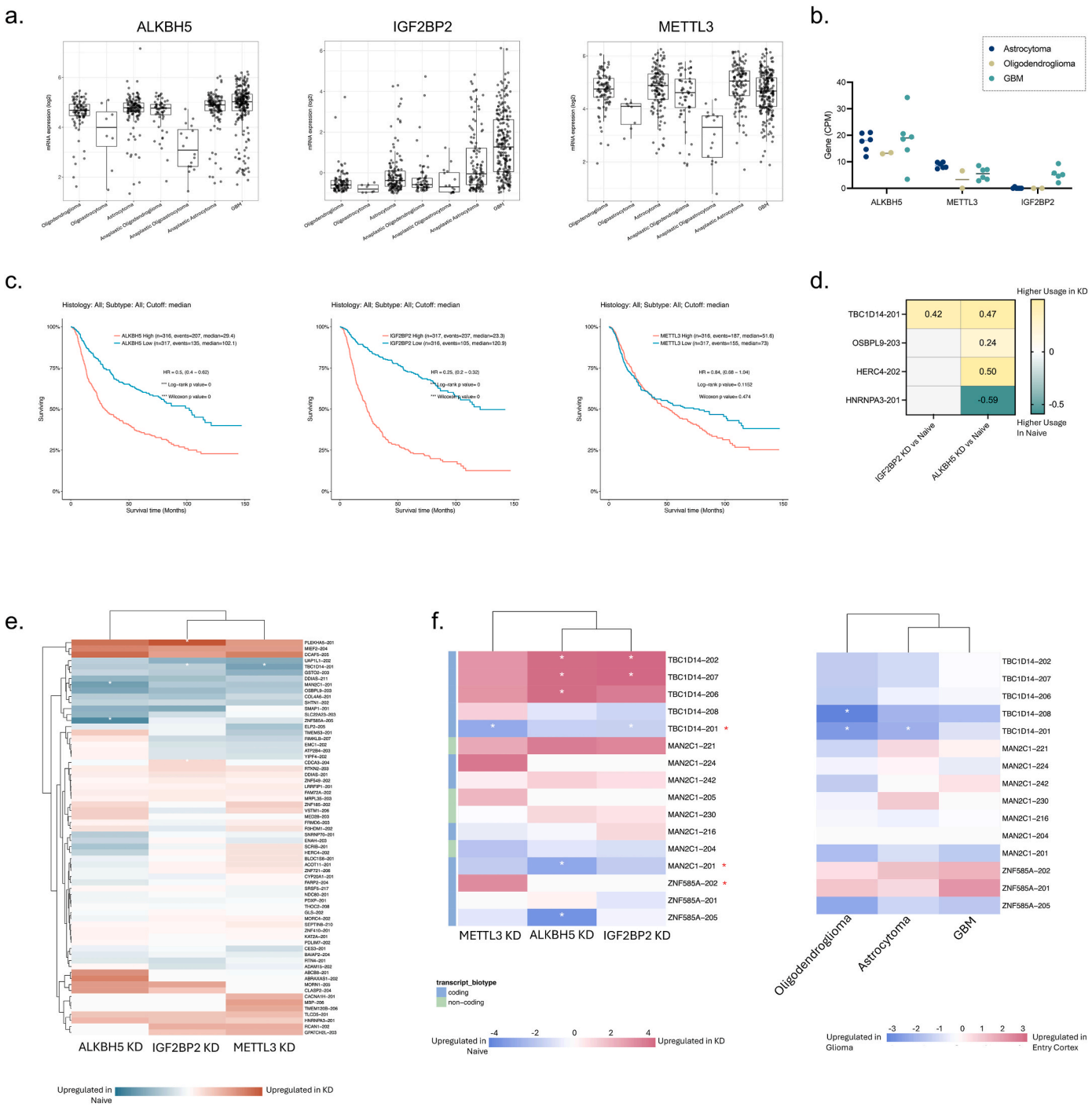

Fig. 7. m6A regulator expression and glioma-associated isoform patterns across datasets. (a) Expression of selected m6A regulators (ALKBH5, IGF2BP2, and METTL3) across glioma tumor classifications using publicly available datasets from GlioVis. (b) RNA-seq–based expression of ALKBH5, IGF2BP2, and METTL3 in patient tumor samples, including astrocytoma (n = 6), oligodendroglioma (n = 2), and glioblastoma (n = 6). (c) Kaplan–Meier survival analyses stratified by expression levels of ALKBH5, IGF2BP2, and METTL3, illustrating associations between regulator expression and patient survival. (d) Heatmap of isoform usage values derived from isoform switching analysis. Isoforms were selected based on dominant glioma-specific switching events curated in the CanIsoNet database. (e) Differential gene expression heatmap of dominant glioma-associated isoforms identified from the CanIsoNet database. (f) Subset of isoforms showing significant differential expression in (e), displayed by gene for glioma cell lines (left) and patient tumor tissues (right), highlighting concordant and context-specific isoform regulation.

Kaplan–Meier analysis in GlioVis further showed that higher ALKBH5 and IGF2BP2 expression was associated with shorter overall survival (Fig. 7c). High ALKBH5 expression corresponded to reduced median survival (29.4 vs 102.1 months; HR = 0.50, 95% CI: 0.40–0.62; log-rank $p < 0.001$), and high IGF2BP2 expression showed a similar association (23.3 vs 120.9 months; HR = 0.25, 95% CI: 0.20–0.32; $p < 0.001$). METTL3 expression was not significantly associated with overall survival (HR = 0.84, 95% CI: 0.68–1.04; $p = 0.115$).

To compare isoform-level findings with external glioma resources, we used CanIsoNet [25], a curated database of annotated isoform switching events in CNS glioblastoma. Overlap with our dataset identified 5 shared switching events between naïve Gli36 cells; one shared

event in IGF2BP2 KD versus naïve, and four shared events in ALKBH5 KD versus naïve (Fig. 7d). We also examined dominant transcripts reported in GBM and assessed their relative expression in our cell-line data. Several dominant transcripts were more highly expressed in naïve glioma cells, including TBC1D14-201 and ZNF585A-205, whereas others were more prominent in specific KD conditions, including MIEF2-204 and CDCA3-204 (Fig. 7e).

We then evaluated the expression of selected dominant transcripts across both cell lines and tumor tissues [26] (Fig. 7f). TBC1D14-201 was increased in the naïve glioma cells relative to METTL3 KD and IGF2BP2 KD, whereas alternative TBC1D14-201 isoforms (202, 207, 206) were enriched in IGF2BP2 KD and ALKBH5 KD. In tumor samples, TBC1D14-201 was elevated in astrocytoma and oligodendroglioma relative to cortex, and TBC1D14-208 was also increased in oligodendroglioma [26]. However, TBC1D14 isoforms (202, 207, 206) did not show significant changes in expression between tumor and cortex [26]. Collectively, these cross-dataset comparisons support the relevance of the observed m6A regulator expression patterns and selected isoform-level changes in glioma.

6. Discussion

In this study, we used long-read direct RNA sequencing to characterize transcriptome-wide m6A patterns in a glioma cell model following perturbation of three core m6A regulators, IGF2BP2, METTL3, and ALKBH5. Across conditions, the overall architecture of m6A remained broadly preserved, including transcript type, positional distribution, and site multiplicity. In contrast, transcript isoform usage showed broader changes and was often accompanied by predicted differences in untranslated regions, coding potential, and transcript structure, whereas differential methylation showed only limited correspondence with gene expression. Together, these findings indicate that m6A regulator perturbation in this model is associated with transcript-level remodeling that is not fully captured by conventional gene-level analyses.

Naïve glioma cells showed relatively greater CDS-associated methylation as compared to the KD conditions. General positional organization of m6A remained recognizable across all conditions, suggesting that perturbation of individual regulators altered regional bias more than the overall framework of m6A distribution. This is broadly consistent with prior work showing that m6A is enriched in the nervous system [3,4,6–8] and can exhibit tissue-, region-, and transcript-specific patterning in brain RNA profiles [5].

The most prominent transcriptomic feature observed after m6A regulator perturbation was widespread isoform switching. Among the knockdown conditions, ALKBH5 KD showed the greatest number of switching events, followed by IGF2BP2 KD and METTL3 KD. Importantly, these isoform-level changes were often more apparent than corresponding gene-level expression changes, and different knockdowns were associated with different classes of high-usage transcripts, including retained intron and nonsense-mediated decay categories. This pattern fits with growing evidence that m6A regulation and alternative splicing [5,21,27–29] are closely interconnected and that perturbation of m6A regulators can be accompanied by broad changes in isoform usage rather than only shifts in total transcript abundance [21,23,27–29]. In glioma specifically, aberrant splicing is increasingly recognized as an important layer of tumor biology and therapeutic vulnerability [30,31]. Our findings are also consistent with prior reports linking IGF2BP2, METTL3, and ALKBH5 to alternative splicing or transcript processing in other biological systems and tumor contexts [21,23,27–29].

The isoform changes that we identified were also associated with predicted structural consequences that support their potential biological relevance. Across knockdown conditions, recurrent features included open reading frame loss, exon loss, domain loss, and shorter coding sequences, while ALKBH5 KD additionally showed enrichment of NMD-sensitive isoforms. Changes in 5′UTR and 3′UTR structure were also observed, particularly in comparisons involving IGF2BP2 KD and ALKBH5 KD. These predicted consequences are relevant because altered UTR structure, coding potential, and domain composition can influence transcript stability, translation, splicing and protein output [1–4], even in the absence of large total gene-expression changes [5,18]. Although these predictions do not demonstrate altered function directly, they indicate that the observed isoform shifts are not merely nominal transcript substitutions and reinforce the value of isoform-resolved analysis in the glioma tumor setting.

A consistent feature across the dataset was the weak relationship between differential methylation and gene expression. Although select pathways and individual transcripts showed parallel shifts, many methylation changes were not accompanied by major gene-expression differences, and many gene-expression changes occurred without a corresponding methylation signal. This limited coupling is not unexpected [32,33], since m6A has been linked not only to transcript abundance, but also to splicing, RNA stability, localization, and translation [1–4]. In that context, the marginal correlation, particularly in METTL3 KD observed here suggests that m6A-associated transcriptomic changes in glioma are not fully summarized by bulk gene-level differential expression, as observed for modified genes associated with apoptosis, MAPK signaling, mTOR signaling, and MYC signaling pathways. This interpretation is also consistent with recent transcript-level studies emphasizing context-dependent and isoform-specific effects of m6A in brain and glioma tissues [5,6,18]. More broadly, our data suggest that relationships between m6A distribution and gene expression may depend on transcript context, regional site localization, and cellular background rather than following a uniform regulatory pattern.

Some of the global methylation patterns observed here were not straightforward when considered solely in terms of canonical writer, reader, and eraser function. Most notably, ALKBH5 knockdown showed the lowest number of detectable m6A-modified sites and transcripts, despite ALKBH5 being an m6A demethylase. As previously shown [23], this apparent paradox underscores the complexity of transcriptome-wide m6A analysis after perturbation of regulatory proteins. The number of detected sites in a given condition may still reflect differences in sequencing outcomes [34,35], including transcript abundance, isoform composition, and sequencing depth, although the m6A modification ratio does account for detected DRACH motifs [34]. In addition, perturbation of a single regulator may trigger broader secondary changes in RNA regulatory networks. Importantly, the ALKBH5-201 transcript was significantly reduced in the ALKBH5 KD condition, while reduction of ALKBH5-202 did not reach statistical significance, suggesting potential compensatory effects on m6A machinery. This type of context dependence is also reflected in the glioma literature, where METTL3, ALKBH5, and IGF2BP2 have each been reported to exert tumor-promoting or context-specific effects [12,15,36] depending on cellular background, transcript targets, and experimental system [19,21,23,27]. For these reasons, global site counts should be interpreted cautiously and not as a simple one-to-one reflection of the expected biochemical direction of individual regulator function.

Our findings also fit within a broader body of glioma literature linking RNA processing factors to tumor biology, particularly splicing programs as major determinants of glioma hierarchy and vulnerability [21,30,37]. For instance, the RNA-binding protein PTBP1 has emerged as a relevant regulator in glioma, with context-dependent associations with tumor state, progression, and ferroptosis [37–39]. In our dataset, expression changes were also observed in several other RNA regulatory factors, including RBFOX1, SRSF family members, DCP2, and EXOSC10. Although we did not functionally test these factors here, their altered expression supports the idea that perturbation of m6A regulators occurs within a broader RNA regulatory network involving splicing and decay machinery. The coordinated expression shifts observed in factors including PTBP1, SRSF family members, DCP2, and EXOSC10 support the interpretation that m6A regulator perturbation is accompanied by broader remodeling of RNA-processing pathways rather than isolated

changes in methylation machinery alone [28–30,40,41]. This interpretation is also compatible with prior work implicating IGF2BP2, WTAP, and ZNF217-related pathways in RNA regulatory control and glioma-associated phenotypes [42,43].

Our findings are further supported by comparisons with public glioma datasets and patient tumor samples. In GlioVis [24], ALKBH5 and IGF2BP2 expression were highest in more aggressive glioma subtypes and were associated with shorter overall survival, while METTL3 showed a distinct expression pattern and no significant survival association. Our tumor cohort study also showed similar broad trends, particularly for IGF2BP2 and METTL3 [26]. At the isoform level, overlap with CanIsoNet [25] and evaluation of selected transcripts such as ZNF585A and TBC1D14 provided additional support that some of the transcript-level differences observed in our cell model are also represented in human glioma datasets. These external comparisons are consistent with prior reports linking IGF2BP2 expression to glioma progression, prognosis, and metabolic regulation [44,45]. At the same time, they should be viewed as supportive rather than definitive validation of the full experimental system.

This study has several limitations. First, the primary experimental system was based on a single glioma cell line and therefore cannot capture the biological diversity of diffuse gliomas defined in the current WHO framework [9,25]. Validation in additional glioma models, including patient-derived glioma stem-like cells and other established cell lines, will be important to establish generalizability and translational relevance. Second, the study relied on siRNA-mediated knockdown rather than genetic knockout, and therefore cannot distinguish direct from indirect effects of regulator perturbation. Third, while isoform switching and predicted structural consequences were prominent, we did not directly test the functional effects of specific isoforms on RNA stability, translation, or protein production, which represents an important direction for future work. Fourth, m6A site identification was based on computational inference from direct RNA sequencing rather than orthogonal site-by-site validation. Finally, variability in sequencing depth across conditions, particularly in the scrambled comparison, limited interpretation of some analyses and required a conservative approach to downstream biological conclusions.

Overall, this study shows that perturbation of m6A regulators in a glioma model is associated with broad transcript-level changes, particularly at the level of isoform usage and predicted transcript structure, whereas changes in global m6A distribution and bulk gene expression are more modest and not tightly coupled. By integrating m6A site prediction with full-length transcript analysis, this work adds an isoform-resolved perspective to the study of RNA regulation in glioma. Future work in additional glioma models and patient-derived systems will be needed to define the biological and functional significance of these transcript-level changes more directly.

AI tools

During the preparation of this work, the authors used ChatGPT for language editing and improvement of readability. The authors reviewed and edited the content as needed and take full responsibility for the final content.

Data

The sequencing and m6A modification data generated in this study are provided in the Supplementary Information and Source Data file. The raw nanopore sequencing data and m6Anet output are available on the Harvard Dataverse at this link: https://dataverse.harvard.edu/dataset.xhtml?persistentId=doi:10.7910/DVN/8TFC38.

Funding

This work is supported by grants R01 CA239078, CA237500, CA291826 (LB). MGN Transformative Scholar (LB), Rappaport Scholar (LB).

CRediT authorship contribution statement

Hanna Lee: Data curation, Formal analysis, Investigation, Methodology, Software, Validation, Visualization, Writing – original draft, Writing – review & editing. **Syeda Maheen Batool:** Data curation, Formal analysis, Investigation, Methodology, Supervision, Validation, Visualization, Writing – original draft, Writing – review & editing. **Ana K. Escobedo:** Data curation, Formal analysis, Methodology, Resources, Software, Validation, Visualization, Writing – original draft, Writing – review & editing. **Denalda Gashi:** Data curation, Methodology, Validation, Writing – review & editing. **Kesli Faber:** Validation, Visualization, Writing – review & editing. **Pavithra Ponnolu:** Validation, Visualization, Writing – review & editing. **Nina R. Barretts:** Validation, Visualization, Writing – review & editing. **Prerna Khanna:** Data curation, Investigation, Validation, Writing – original draft. **Kase D. Haas:** Data curation, Methodology, Validation, Writing – original draft. **Tiffaney Hsia:** Data curation, Formal analysis, Methodology, Visualization, Writing – original draft. **Bob S. Carter:** Investigation, Project administration, Resources, Writing – review & editing. **Leonora Balaj:** Conceptualization, Data curation, Formal analysis, Funding acquisition, Investigation, Methodology, Project administration, Resources, Software, Supervision, Validation, Visualization, Writing – original draft, Writing – review & editing.

Declaration of competing interest

The authors declare that they have no known competing financial interests or personal relationships that could have appeared to influence the work reported in this paper.

Appendix A. Supplementary data

Supplementary data to this article can be found online at https://doi.org/10.1016/j.bbrep.2026.102614.

Data availability

Data is share online at the Harvard Dataverse and a link is provided in the manuscript

References

[1] J. Akhtar, M. Lugoboni, G. Junion, M6a RNA modification in transcription regulation, Transcription 12 (2021) 266–276, https://doi.org/10.1080/21541264.2022.2057177.
[2] W. Huang, T.-Q. Chen, K. Fang, Z.-C. Zeng, H. Ye, Y.-Q. Chen, N6-methyladenosine methyltransferases: functions, regulation, and clinical potential, J. Hematol. Oncol. 14 (2021) 117, https://doi.org/10.1186/s13045-021-01129-8.
[3] L. Jiang, X. Li, S. Wang, Z. Yuan, J. Cheng, The role and regulatory mechanism of M6A methylation in the nervous system, Front. Genet. 13 (2022), https://doi.org/10.3389/fgene.2022.962774.
[4] Y. Fan, X. Lv, Z. Chen, Y. Peng, M. Zhang, M6A methylation: critical roles in aging and neurological diseases, Front. Mol. Neurosci. 16 (2023), https://doi.org/10.3389/fnmol.2023.1102147.
[5] J. Gleeson, S.U. Madugalle, C.Y. Wan, C. McLean, T.W. Bredy, R. De Paoli-Iseppi, et al., Isoform-level profiling of M6a epitranscriptomic signatures in human brain, Sci. Adv. 11 (2025), https://doi.org/10.1126/sciadv.adp0783.
[6] A.K. Chokkalla, S.L. Mehta, R. Vemuganti, Epitranscriptomic regulation by M6a RNA methylation in brain development and diseases, J. Cereb. Blood Flow Metab. 40 (2020) 2331–2349, https://doi.org/10.1177/0271678x20960033.
[7] B. Du, Y. Zhang, M. Liang, Z. Du, H. Li, C. Fan, et al., N6-methyladenosine (M6A) modification and its clinical relevance in cognitive dysfunctions, Aging 13 (2021) 20716–20737, https://doi.org/10.18632/aging.203457.
[8] J. Yu, Y. She, S.-J. Ji, M6A modification in mammalian nervous system development, functions, disorders, and injuries, Front. Cell Dev. Biol. 9 (2021), https://doi.org/10.3389/fcell.2021.679662.
[9] D.N. Louis, A. Perry, P. Wesseling, D.J. Brat, I.A. Cree, D. Figarella-Branger, et al., The 2021 who classification of tumors of the central nervous system: a summary, Neuro Oncol. 23 (2021) 1231–1251, https://doi.org/10.1093/neuonc/noab106.

[10] S. Xu, L. Tang, X. Li, F. Fan, Z. Liu, Immunotherapy for glioma: current management and future application, Cancer Lett. 476 (2020) 1–12, https://doi.org/10.1016/j.canlet.2020.02.002.
[11] S. Mohammed, D. M, A. T, Survival and quality of life analysis in glioblastoma multiforme with adjuvant chemoradiotherapy: a retrospective study, Rep. Practical Oncol. Radiother. 27 (2022) 1026–1036, https://doi.org/10.5603/rpor.a2022.0113.
[12] J.-J. Chen, T.-Z. Lu, T. Wang, W.-H. Yan, F.-Y. Zhong, X.-H. Qu, et al., The m6A reader HNRNPC promotes glioma progression by enhancing the stability of IRAK1 mRNA through the MAPK pathway, Cell Death Dis. 15 (2024), https://doi.org/10.1038/s41419-024-06736-0.
[13] Y. Zhang, X. Geng, Q. Li, J. Xu, Y. Tan, M. Xiao, et al., m6A modification in RNA: biogenesis, functions and roles in gliomas, J. Exp. Clin. Cancer Res. 39 (2020) 192, https://doi.org/10.1186/s13046-020-01706-8.
[14] J. Yin, F. Ding, Z. Cheng, X. Ge, Y. Li, A. Zeng, et al., METTL3-mediated m6A modification of LINC00839 maintains glioma stem cells and radiation resistance by activating Wnt/β-catenin signaling, Cell Death Dis. 14 (2023), https://doi.org/10.1038/s41419-023-05933-7.
[15] A. Visvanathan, V. Patil, A. Arora, A.S. Hegde, A. Arivazhagan, V. Santosh, et al., Essential role of METTL3-mediated M6A modification in glioma stem-like cells maintenance and radioresistance, Oncogene 37 (2017) 522–533, https://doi.org/10.1038/onc.2017.351.
[16] M.L. Suvà, E. Rheinbay, S.M. Gillespie, A.P. Patel, H. Wakimoto, S.D. Rabkin, et al., Reconstructing and reprogramming the tumor-propagating potential of glioblastoma stem-like cells, Cell 157 (2014) 580–594, https://doi.org/10.1016/j.cell.2014.02.030.
[17] F. Yuan, X. Cai, Z. Cong, Y. Wang, Y. Geng, Y. Aili, et al., Roles of the M6A modification of RNA in the glioblastoma microenvironment as revealed by single-cell analyses, Front. Immunol. 13 (2022), https://doi.org/10.3389/fimmu.2022.798583.
[18] G. Steponaitis, R. Dragunaite, R. Stakaitis, A. Sharma, A. Tamasauskas, D. Skiriute, m6A-lncRNA landscape highlights reduced levels of m6A modification in glioblastoma as compared to low-grade glioma, Mol Med 31 (2025) 195, https://doi.org/10.1186/s10020-025-01254-x.
[19] Q. Cui, H. Shi, P. Ye, L. Li, Q. Qu, G. Sun, et al., mA RNA methylation regulates the self-renewal and tumorigenesis of glioblastoma stem cells, Cell Rep. 18 (2017) 2622–2634, https://doi.org/10.1016/j.celrep.2017.02.059.
[20] K. Vitting-Seerup, A. Sandelin, IsoformSwitchAnalyzeR: analysis of changes in genome-wide patterns of alternative splicing and its functional consequences, Bioinformatics 35 (2019) 4469–4471, https://doi.org/10.1093/bioinformatics/btz247.
[21] W. Liu, Y. Liu, H. Li, S. Wang, P. Chen, Z. Liu, et al., IGF2BP2 orchestrates global expression and alternative splicing profiles associated with glioblastoma development in U251 cells, Transl. Oncol. 51 (2025) 102177, https://doi.org/10.1016/j.tranon.2024.102177.
[22] H. Lee, D. Gashi, S.M. Batool, A.K. Escobedo, A.A. Petti, B.S. Carter, et al., M6anetanalyzer: an R toolkit for post-processing of M6A sites detected by m6anet, Bioinform. Adv. 6 (2026), https://doi.org/10.1093/bioadv/vbag089.
[23] C. Tang, R. Klukovich, H. Peng, Z. Wang, T. Yu, Y. Zhang, et al., Alkbh5-dependent M6A Demethylation Controls Splicing and Stability of Long 3′-UTR Mrnas in Male Germ Cells, 115, Proceedings of the National Academy of Sciences, 2017, https://doi.org/10.1073/pnas.1717794115.
[24] R.L. Bowman, Q. Wang, A. Carro, R.G.W. Verhaak, M. Squatrito, GlioVis data portal for visualization and analysis of brain tumor expression datasets, Neuro Oncol. 19 (2017) 139–141, https://doi.org/10.1093/neuonc/now247.
[25] T. Karakulak, D. Szklarczyk, C.C. Saylan, H. Moch, C. von Mering, A. Kahraman, CanIsoNet: a database to study the functional impact of isoform switching events in diseases, Bioinform. Adv. 3 (2023), https://doi.org/10.1093/bioadv/vbad050.
[26] S.M. Batool, S.M. Khan, K. Muralidharan, et al., IDH1-dependent m6A methylation defines transcriptomic heterogeneity in glioma, medRxiv (2025), https://doi.org/10.1101/2024.09.24.24314089.
[27] Y. Kim, S. Shin, S. Kwon, K. Moon, S.-V. Baek, A. Jo, et al., METTL3 regulates alternative splicing of cell cycle-related genes via crosstalk between mRNA m6A modifications and splicing factors, Am. J. Cancer Res. 13 (4) (2023) 1443–1456. PubMed PMID: 37168328; PubMed Central PMCID: PMC10164804.
[28] Z. Zhu, F. Huo, J. Zhang, H. Shan, D. Pei, Crosstalk between M6A modification and alternative splicing during cancer progression, Clin. Transl. Med. 13 (2023), https://doi.org/10.1002/ctm2.1460.
[29] M. Mehravar, J.J.-L. Wong, Interplay between N-adenosine RNA methylation and mrna splicing, Curr. Opin. Genet. Dev. 87 (2024) 102211, https://doi.org/10.1016/j.gde.2024.102211.
[30] X. Song, D. Tiek, S. Miki, T. Huang, M. Lu, A. Goenka, et al., RNA splicing analysis deciphers developmental hierarchies and reveals therapeutic targets in adult glioma, J. Clin. Investig. 134 (2024), https://doi.org/10.1172/jci173789.
[31] Mrid R. Ben, S. El Guendouzi, M. Mineo, R. El Fatimy, The emerging roles of aberrant alternative splicing in glioma, Cell Death Discov. 11 (2025), https://doi.org/10.1038/s41420-025-02323-0.
[32] C.M. Fitzsimmons, P.J. Batista, It's complicated… M6A-dependent regulation of gene expression in cancer, Biochimica et Biophysica Acta (BBA) - Gene Regulatory Mechanisms 1862 (2019) 382–393, https://doi.org/10.1016/j.bbagrm.2018.09.010.
[33] Z.-L. Lin, P.-P. Yu, B.-L. Ye, Cis-regulation analysis of RNA M6A methylation and gene expression in colorectal cancer, Front. Genet. 16 (2025), https://doi.org/10.3389/fgene.2025.1622957.
[34] C. Hendra, P.N. Pratanwanich, Y.K. Wan, W.S. Goh, A. Thiery, J. Göke, Detection of M6A from direct RNA sequencing using a multiple instance learning framework, Nat. Methods 19 (2022) 1590–1598, https://doi.org/10.1038/s41592-022-01666-1.
[35] J.F. Liu, B.R. Hawley, L.S. Nicholson, S.R. Jaffrey, Decoding m6am by simultaneous transcription-start mapping and methylation quantification, eLife 13 (2025), https://doi.org/10.7554/elife.104139.3.
[36] A. Visvanathan, V. Patil, S. Abdulla, J. Hoheisel, K. Somasundaram, N6-methyladenosine landscape of glioma stem-like cells: METTL3 is essential for the expression of actively transcribed genes and sustenance of the oncogenic signaling, Genes 10 (2019) 141, https://doi.org/10.3390/genes10020141.
[37] J. Yang, J. Feng, J. Lv, X. Chu, Y. Wei, Y. Zhang, et al., PTBP1-mediated Repression of Neuron-specific CDC42 Splicing Constitutes a Genomic alteration-independent, Developmentally Conserved Vulnerability in IDH-wildtype Glioblastoma, vol. 24, Funct Integr Genomics, 2024, p. 135, https://doi.org/10.1007/s10142-024-01412-0.
[38] Z. Ye, Y. Zhong, Z. Zhang, Pan-cancer multi-omics analysis of PTBP1 reveals it as an inflammatory, progressive and prognostic marker in glioma, Sci. Rep. 14 (2024), https://doi.org/10.1038/s41598-024-64979-5.
[39] J. Sun, B. Xue, T. Sun, X. Xu, D. Zhang, Z. Shan, et al., PTBP1 acts as a tumor suppressor in glioma by promoting HMOX1-dependent ferroptosis, Biochem. Pharmacol. 239 (2025) 117041, https://doi.org/10.1016/j.bcp.2025.117041.
[40] J. Domingo-Prim, M. Endara-Coll, F. Bonath, S. Jimeno, R. Prados-Carvajal, M. R. Friedländer, et al., EXOSC10 is required for RPA assembly and controlled DNA end resection at DNA double-strand breaks, Nat. Commun. 10 (2019), https://doi.org/10.1038/s41467-019-10153-9.
[41] Y. Mei, Q. Lv, Z. Tan, Z. Zhang, Y. Ji, S. Chen, et al., Decapping enzyme 2 is a novel immune-related biomarker that predicts poor prognosis in glioma, Biotechnol. Genet. Eng. Rev. 40 (2024) 4262–4283, https://doi.org/10.1080/02648725.2023.2209409.
[42] H. Liu, S. Qin, C. Liu, L. Jiang, C. Li, J. Yang, et al., M6A reader IGF2BP2-stabilized CASC9 accelerates glioblastoma aerobic glycolysis by enhancing HK2 mrna stability, Cell Death Discov. 7 (2021), https://doi.org/10.1038/s41420-021-00674-y.
[43] D.-F. Lee, M.J. Walsh, F. Aguiló, ZNF217/ZFP217 meets chromatin and RNA, Trends Biochem. Sci. 41 (2016) 986–988, https://doi.org/10.1016/j.tibs.2016.07.013.
[44] H.-L. Zhou, D.-D. Chen, X.-L. Li, Pan-cancer analysis identified IGF2BP2 as a potential prognostic biomarker for multiple tumor types, Egypt. J. Med. Hum. Genet. 25 (2024), https://doi.org/10.1186/s43042-023-00468-0.
[45] N. Li, L. Deng, Y. Zhang, X. Tang, B. Lei, Q. Zhang, IGF2BP2 modulates autophagy and serves as a prognostic marker in glioma, Ibrain 10 (2024) 19–33, https://doi.org/10.1002/ibra.12150.